

Measurements of branching fractions and CP asymmetries and studies of angular distributions for $B \rightarrow \phi\phi K$ decays

J. P. Lees,¹ V. Poireau,¹ E. Prencipe,¹ V. Tisserand,¹ J. Garra Tico,² E. Grauges,² M. Martinelli,^{3a,3b} D. A. Milanes,^{3a} A. Palano,^{3a,3b} M. Pappagallo,^{3a,3b} G. Eigen,⁴ B. Stugu,⁴ L. Sun,⁴ D. N. Brown,⁵ L. T. Kerth,⁵ Yu. G. Kolomensky,⁵ G. Lynch,⁵ H. Koch,⁶ T. Schroeder,⁶ D. J. Asgeirsson,⁷ C. Hearty,⁷ T. S. Mattison,⁷ J. A. McKenna,⁷ A. Khan,⁸ V. E. Blinov,⁹ A. R. Buzykaev,⁹ V. P. Druzhinin,⁹ V. B. Golubev,⁹ E. A. Kravchenko,⁹ A. P. Onuchin,⁹ S. I. Serednyakov,⁹ Yu. I. Skovpen,⁹ E. P. Solodov,⁹ K. Yu. Todyshev,⁹ A. N. Yushkov,⁹ M. Bondioli,¹⁰ S. Curry,¹⁰ D. Kirkby,¹⁰ A. J. Lankford,¹⁰ M. Mandelkern,¹⁰ D. P. Stoker,¹⁰ H. Atmacan,¹¹ J. W. Gary,¹¹ F. Liu,¹¹ O. Long,¹¹ G. M. Vitug,¹¹ C. Campagnari,¹² T. M. Hong,¹² D. Kovalskyi,¹² J. D. Richman,¹² C. A. West,¹² A. M. Eisner,¹³ J. Kroseberg,¹³ W. S. Lockman,¹³ A. J. Martinez,¹³ T. Schalk,¹³ B. A. Schumm,¹³ A. Seiden,¹³ C. H. Cheng,¹⁴ D. A. Doll,¹⁴ B. Echenard,¹⁴ K. T. Flood,¹⁴ D. G. Hitlin,¹⁴ P. Ongmongkolkul,¹⁴ F. C. Porter,¹⁴ A. Y. Rakitin,¹⁴ R. Andreassen,¹⁵ M. S. Dubrovin,¹⁵ B. T. Meadows,¹⁵ M. D. Sokoloff,¹⁵ P. C. Bloom,¹⁶ W. T. Ford,¹⁶ A. Gaz,¹⁶ M. Nagel,¹⁶ U. Nauenberg,¹⁶ J. G. Smith,¹⁶ S. R. Wagner,¹⁶ R. Ayad,^{17,*} W. H. Toki,¹⁷ B. Spaan,¹⁸ M. J. Kobel,¹⁹ K. R. Schubert,¹⁹ R. Schwierz,¹⁹ D. Bernard,²⁰ M. Verderi,²⁰ P. J. Clark,²¹ S. Playfer,²¹ J. E. Watson,²¹ D. Bettoni,^{22a} C. Bozzi,^{22a} R. Calabrese,^{22a,22b} G. Cibinetto,^{22a,22b} E. Fioravanti,^{22a,22b} I. Garzia,^{22a,22b} E. Luppi,^{22a,22b} M. Menerato,^{22a,22b} M. Negrini,^{22a,22b} L. Piemontese,^{22a} R. Baldini-Ferroli,²³ A. Calcaterra,²³ R. de Sangro,²³ G. Finocchiaro,²³ M. Nicolaci,²³ S. Pacetti,²³ P. Patteri,²³ I. M. Peruzzi,^{23,†} M. Piccolo,²³ M. Rama,²³ A. Zallo,²³ R. Contri,^{24a,24b} E. Guido,^{24a,24b} M. Lo Vetere,^{24a,24b} M. R. Monge,^{24a,24b} S. Passaggio,^{24a} C. Patrignani,^{24a,24b} E. Robutti,^{24a} B. Bhuyan,²⁵ V. Prasad,²⁵ C. L. Lee,²⁶ M. Morii,²⁶ A. J. Edwards,²⁷ A. Adametz,²⁸ J. Marks,²⁸ U. Uwer,²⁸ F. U. Bernlochner,²⁹ M. Ebert,²⁹ H. M. Lacker,²⁹ T. Lueck,²⁹ P. D. Dauncey,³⁰ M. Tibbetts,³⁰ P. K. Behera,³¹ U. Mallik,³¹ C. Chen,³² J. Cochran,³² H. B. Crawley,³² W. T. Meyer,³² S. Prell,³² E. I. Rosenberg,³² A. E. Rubin,³² A. V. Gritsan,³³ Z. J. Guo,³³ N. Arnaud,³⁴ M. Davier,³⁴ D. Derkach,³⁴ G. Grosdidier,³⁴ F. Le Diberder,³⁴ A. M. Lutz,³⁴ B. Malaescu,³⁴ P. Roudeau,³⁴ M. H. Schune,³⁴ A. Stocchi,³⁴ G. Wormser,³⁴ D. J. Lange,³⁵ D. M. Wright,³⁵ I. Bingham,³⁶ C. A. Chavez,³⁶ J. P. Coleman,³⁶ J. R. Fry,³⁶ E. Gabathuler,³⁶ D. E. Hutchcroft,³⁶ D. J. Payne,³⁶ C. Touramanis,³⁶ A. J. Bevan,³⁷ F. Di Lodovico,³⁷ R. Sacco,³⁷ M. Sigamani,³⁷ G. Cowan,³⁸ S. Paramesvaran,³⁸ D. N. Brown,³⁹ C. L. Davis,³⁹ A. G. Denig,⁴⁰ M. Fritsch,⁴⁰ W. Gradl,⁴⁰ A. Hafner,⁴⁰ K. E. Alwyn,⁴¹ D. Bailey,⁴¹ R. J. Barlow,⁴¹ G. Jackson,⁴¹ G. D. Lafferty,⁴¹ R. Cenci,⁴² B. Hamilton,⁴² A. Jawahery,⁴² D. A. Roberts,⁴² G. Simi,⁴² C. Dallapiccola,⁴³ E. Salvati,⁴³ R. Cowan,⁴⁴ D. Dujmic,⁴⁴ G. Sciolla,⁴⁴ D. Lindemann,⁴⁵ P. M. Patel,⁴⁵ S. H. Robertson,⁴⁵ M. Schram,⁴⁵ P. Biassoni,^{46a,46b} A. Lazzaro,^{46a,46b} V. Lombardo,^{46a} F. Palombo,^{46a,46b} S. Stracka,^{46a,46b} L. Cremaldi,⁴⁷ R. Godang,^{47,‡} R. Kroeger,⁴⁷ P. Sonnek,⁴⁷ D. J. Summers,⁴⁷ X. Nguyen,⁴⁸ P. Taras,⁴⁸ G. De Nardo,^{49a,49b} D. Monorchio,^{49a,49b} G. Onorato,^{49a,49b} C. Sciacca,^{49a,49b} G. Raven,⁵⁰ H. L. Snoek,⁵⁰ C. P. Jessop,⁵¹ K. J. Knoepfel,⁵¹ J. M. LoSecco,⁵¹ W. F. Wang,⁵¹ K. Honscheid,⁵² R. Kass,⁵² J. Brau,⁵³ R. Frey,⁵³ N. B. Sinev,⁵³ D. Strom,⁵³ E. Torrence,⁵³ E. Feltresi,^{54a,54b} N. Gagliardi,^{54a,54b} M. Margoni,^{54a,54b} M. Morandin,^{54a} M. Posocco,^{54a} M. Rotondo,^{54a,54b} F. Simonetto,^{54a,54b} R. Stroili,^{54a,54b} E. Ben-Haim,⁵⁵ M. Bomben,⁵⁵ G. R. Bonneaud,⁵⁵ H. Briand,⁵⁵ G. Calderini,⁵⁵ J. Chauveau,⁵⁵ O. Hamon,⁵⁵ Ph. Leruste,⁵⁵ G. Marchiori,⁵⁵ J. Ocariz,⁵⁵ S. Sitt,⁵⁵ M. Biasini,^{56a,56b} E. Manoni,^{56a,56b} A. Rossi,^{56a,56b} C. Angelini,^{57a,57b} G. Batignani,^{57a,57b} S. Bettarini,^{57a,57b} M. Carpinelli,^{57a,57b,§} G. Casarosa,^{57a,57b} A. Cervelli,^{57a,57b} F. Forti,^{57a,57b} M. A. Giorgi,^{57a,57c} A. Lusiani,^{57a,57c} N. Neri,^{57a,57b} B. Oberhof,^{57a,57b} E. Paoloni,^{57a} A. Perez,^{57a} G. Rizzo,^{57a,57b} J. J. Walsh,^{57a} D. Lopes Pegna,⁵⁸ C. Lu,⁵⁸ J. Olsen,⁵⁸ A. J. S. Smith,⁵⁸ A. V. Telnov,⁵⁸ F. Anulli,^{59a} G. Cavoto,^{59a,59b} R. Faccini,^{59a} F. Ferrarotto,^{59a,59b} F. Ferroni,^{59a,59b} M. Gaspero,^{59a} L. Li Gioi,^{59a} M. A. Mazzoni,^{59a} G. Piredda,^{59a} C. Büniger,⁶⁰ T. Hartmann,⁶⁰ T. Leddig,⁶⁰ H. Schröder,⁶⁰ R. Waldi,⁶⁰ T. Auye, ⁶¹ E. O. Olaiya,⁶¹ F. F. Wilson,⁶¹ S. Emery,⁶² G. Hamel de Monchenault,⁶² G. Vasseur,⁶² Ch. Yèche,⁶² D. Aston,⁶³ D. J. Bard,⁶³ R. Bartoldus,⁶³ J. F. Benitez,⁶³ C. Cartaro,⁶³ M. R. Convery,⁶³ J. Dorfan,⁶³ G. P. Dubois-Felsmann,⁶³ W. Dunwoodie,⁶³ R. C. Field,⁶³ M. Franco Sevilla,⁶³ B. G. Fulsom,⁶³ A. M. Gabareen,⁶³ M. T. Graham,⁶³ P. Grenier,⁶³ C. Hast,⁶³ W. R. Innes,⁶³ M. H. Kelsey,⁶³ H. Kim,⁶³ P. Kim,⁶³ M. L. Kocian,⁶³ D. W. G. S. Leith,⁶³ P. Lewis,⁶³ S. Li,⁶³ B. Lindquist,⁶³ S. Luitz,⁶³ V. Luth,⁶³ H. L. Lynch,⁶³ D. B. MacFarlane,⁶³ D. R. Muller,⁶³ H. Neal,⁶³ S. Nelson,⁶³ I. Ofte,⁶³ M. Perl,⁶³ T. Pulliam,⁶³ B. N. Ratcliff,⁶³ A. Roodman,⁶³ A. A. Salnikov,⁶³ V. Santoro,⁶³ R. H. Schindler,⁶³ A. Snyder,⁶³ D. Su,⁶³ M. K. Sullivan,⁶³ J. Va'vra,⁶³ A. P. Wagner,⁶³ M. Weaver,⁶³ W. J. Wisniewski,⁶³ M. Wittgen,⁶³ D. H. Wright,⁶³ H. W. Wulsin,⁶³ A. K. Yarritu,⁶³ C. C. Young,⁶³ V. Ziegler,⁶³ W. Park,⁶⁴ M. V. Purohit,⁶⁴ R. M. White,⁶⁴ J. R. Wilson,⁶⁴ A. Randle-Conde,⁶⁵ S. J. Sekula,⁶⁵ M. Bellis,⁶⁶ P. R. Burchat,⁶⁶ T. S. Miyashita,⁶⁶ M. S. Alam,⁶⁷ J. A. Ernst,⁶⁷ R. Gorodeisky,⁶⁸ N. Guttman,⁶⁸ D. R. Peimer,⁶⁸ A. Soffer,⁶⁸ P. Lund,⁶⁹ S. M. Spanier,⁶⁹ R. Eckmann,⁷⁰ J. L. Ritchie,⁷⁰ A. M. Ruland,⁷⁰ C. J. Schilling,⁷⁰ R. F. Schwitters,⁷⁰ B. C. Wray,⁷⁰ J. M. Izen,⁷¹ X. C. Lou,⁷¹ F. Bianchi,^{72a,72b}

- D. Gamba,^{72a,72b} L. Lanceri,^{73a,73b} L. Vitale,^{73a,73b} N. Lopez-March,⁷⁴ F. Martinez-Vidal,⁷⁴ A. Oyanguren,⁷⁴ H. Ahmed,⁷⁵ J. Albert,⁷⁵ Sw. Banerjee,⁷⁵ H. H. F. Choi,⁷⁵ G. J. King,⁷⁵ R. Kowalewski,⁷⁵ M. J. Lewczuk,⁷⁵ C. Lindsay,⁷⁵ I. M. Nugent,⁷⁵ J. M. Roney,⁷⁵ R. J. Sobie,⁷⁵ T. J. Gershon,⁷⁶ P. F. Harrison,⁷⁶ T. E. Latham,⁷⁶ E. M. T. Puccio,⁷⁶ H. R. Band,⁷⁷ S. Dasu,⁷⁷ Y. Pan,⁷⁷ R. Prepost,⁷⁷ C. O. Vuosalo,⁷⁷ and S. L. Wu⁷⁷
- ¹*Laboratoire d'Annecy-le-Vieux de Physique des Particules (LAPP), Université de Savoie, CNRS/IN2P3, F-74941 Annecy-Le-Vieux, France*
- ²*Universitat de Barcelona, Facultat de Física, Departament ECM, E-08028 Barcelona, Spain*
- ^{3a}*INFN Sezione di Bari, I-70126 Bari, Italy*
- ^{3b}*Dipartimento di Fisica, Università di Bari, I-70126 Bari, Italy*
- ⁴*University of Bergen, Institute of Physics, N-5007 Bergen, Norway*
- ⁵*Lawrence Berkeley National Laboratory and University of California, Berkeley, California 94720, USA*
- ⁶*Ruhr Universität Bochum, Institut für Experimentalphysik 1, D-44780 Bochum, Germany*
- ⁷*University of British Columbia, Vancouver, British Columbia, Canada V6T 1Z1*
- ⁸*Brunel University, Uxbridge, Middlesex UB8 3PH, United Kingdom*
- ⁹*Budker Institute of Nuclear Physics, Novosibirsk 630090, Russia*
- ¹⁰*University of California at Irvine, Irvine, California 92697, USA*
- ¹¹*University of California at Riverside, Riverside, California 92521, USA*
- ¹²*University of California at Santa Barbara, Santa Barbara, California 93106, USA*
- ¹³*University of California at Santa Cruz, Institute for Particle Physics, Santa Cruz, California 95064, USA*
- ¹⁴*California Institute of Technology, Pasadena, California 91125, USA*
- ¹⁵*University of Cincinnati, Cincinnati, Ohio 45221, USA*
- ¹⁶*University of Colorado, Boulder, Colorado 80309, USA*
- ¹⁷*Colorado State University, Fort Collins, Colorado 80523, USA*
- ¹⁸*Technische Universität Dortmund, Fakultät Physik, D-44221 Dortmund, Germany*
- ¹⁹*Technische Universität Dresden, Institut für Kern- und Teilchenphysik, D-01062 Dresden, Germany*
- ²⁰*Laboratoire Leprince-Ringuet, CNRS/IN2P3, Ecole Polytechnique, F-91128 Palaiseau, France*
- ²¹*University of Edinburgh, Edinburgh EH9 3JZ, United Kingdom*
- ^{22a}*INFN Sezione di Ferrara; Dipartimento di Fisica, I-44100 Ferrara, Italy*
- ^{22b}*Dipartimento di Fisica, Università di Ferrara, I-44100 Ferrara, Italy*
- ²³*INFN Laboratori Nazionali di Frascati, I-00044 Frascati, Italy*
- ^{24a}*INFN Sezione di Genova, I-16146 Genova, Italy*
- ^{24b}*Dipartimento di Fisica, Università di Genova, I-16146 Genova, Italy*
- ²⁵*Indian Institute of Technology Guwahati, Guwahati, Assam, 781 039, India*
- ²⁶*Harvard University, Cambridge, Massachusetts 02138, USA*
- ²⁷*Harvey Mudd College, Claremont, California 91711 USA*
- ²⁸*Universität Heidelberg, Physikalisches Institut, Philosophenweg 12, D-69120 Heidelberg, Germany*
- ²⁹*Humboldt-Universität zu Berlin, Institut für Physik, Newtonstr. 15, D-12489 Berlin, Germany*
- ³⁰*Imperial College London, London, SW7 2AZ, United Kingdom*
- ³¹*University of Iowa, Iowa City, Iowa 52242, USA*
- ³²*Iowa State University, Ames, Iowa 50011-3160, USA*
- ³³*Johns Hopkins University, Baltimore, Maryland 21218, USA*
- ³⁴*Laboratoire de l'Accélérateur Linéaire, IN2P3/CNRS et Université Paris-Sud 11, Centre Scientifique d'Orsay, B. P. 34, F-91898 Orsay Cedex, France*
- ³⁵*Lawrence Livermore National Laboratory, Livermore, California 94550, USA*
- ³⁶*University of Liverpool, Liverpool L69 7ZE, United Kingdom*
- ³⁷*Queen Mary, University of London, London, E1 4NS, United Kingdom*
- ³⁸*University of London, Royal Holloway and Bedford New College, Egham, Surrey TW20 0EX, United Kingdom*
- ³⁹*University of Louisville, Louisville, Kentucky 40292, USA*
- ⁴⁰*Johannes Gutenberg-Universität Mainz, Institut für Kernphysik, D-55099 Mainz, Germany*
- ⁴¹*University of Manchester, Manchester M13 9PL, United Kingdom*
- ⁴²*University of Maryland, College Park, Maryland 20742, USA*
- ⁴³*University of Massachusetts, Amherst, Massachusetts 01003, USA*
- ⁴⁴*Massachusetts Institute of Technology, Laboratory for Nuclear Science, Cambridge, Massachusetts 02139, USA*
- ⁴⁵*McGill University, Montréal, Québec, Canada H3A 2T8*
- ^{46a}*INFN Sezione di Milano; I-20133 Milano, Italy*
- ^{46b}*Dipartimento di Fisica, Università di Milano, I-20133 Milano, Italy*
- ⁴⁷*University of Mississippi, University, Mississippi 38677, USA*
- ⁴⁸*Université de Montréal, Physique des Particules, Montréal, Québec, Canada H3C 3J7*
- ^{49a}*INFN Sezione di Napoli, I-80126 Napoli, Italy*

- ^{49b}*Dipartimento di Scienze Fisiche, Università di Napoli Federico II, I-80126 Napoli, Italy*
⁵⁰*NIKHEF, National Institute for Nuclear Physics and High Energy Physics, NL-1009 DB Amsterdam, The Netherlands*
⁵¹*University of Notre Dame, Notre Dame, Indiana 46556, USA*
⁵²*Ohio State University, Columbus, Ohio 43210, USA*
⁵³*University of Oregon, Eugene, Oregon 97403, USA*
^{54a}*INFN Sezione di Padova, I-35131 Padova, Italy*
^{54b}*Dipartimento di Fisica, Università di Padova, I-35131 Padova, Italy*
⁵⁵*Laboratoire de Physique Nucléaire et de Hautes Energies, IN2P3/CNRS, Université Pierre et Marie Curie-Paris6, Université Denis Diderot-Paris7, F-75252 Paris, France*
^{56a}*INFN Sezione di Perugia, I-06100 Perugia, Italy*
^{56b}*Dipartimento di Fisica, Università di Perugia, I-06100 Perugia, Italy*
^{57a}*INFN Sezione di Pisa, I-56127 Pisa, Italy*
^{57b}*Dipartimento di Fisica, Università di Pisa, I-56127 Pisa, Italy*
^{57c}*Scuola Normale Superiore di Pisa, I-56127 Pisa, Italy*
⁵⁸*Princeton University, Princeton, New Jersey 08544, USA*
^{59a}*INFN Sezione di Roma, I-00185 Roma, Italy*
^{59b}*Dipartimento di Fisica, Università di Roma La Sapienza, I-00185 Roma, Italy*
⁶⁰*Universität Rostock, D-18051 Rostock, Germany*
⁶¹*Rutherford Appleton Laboratory, Chilton, Didcot, Oxon, OX11 0QX, United Kingdom*
⁶²*CEA, Ifu, SPP, Centre de Saclay, F-91191 Gif-sur-Yvette, France*
⁶³*SLAC National Accelerator Laboratory, Stanford, California 94309, USA*
⁶⁴*University of South Carolina, Columbia, South Carolina 29208, USA*
⁶⁵*Southern Methodist University, Dallas, Texas 75275, USA*
⁶⁶*Stanford University, Stanford, California 94305-4060, USA*
⁶⁷*State University of New York, Albany, New York 12222, USA*
⁶⁸*Tel Aviv University, School of Physics and Astronomy, Tel Aviv, 69978, Israel*
⁶⁹*University of Tennessee, Knoxville, Tennessee 37996, USA*
⁷⁰*University of Texas at Austin, Austin, Texas 78712, USA*
⁷¹*University of Texas at Dallas, Richardson, Texas 75083, USA*
^{72a}*INFN Sezione di Torino, I-10125 Torino, Italy*
^{72b}*Dipartimento di Fisica Sperimentale, Università di Torino, I-10125 Torino, Italy*
^{73a}*INFN Sezione di Trieste, I-34127 Trieste, Italy*
^{73b}*Dipartimento di Fisica, Università di Trieste, I-34127 Trieste, Italy*
⁷⁴*IFIC, Universitat de Valencia-CSIC, E-46071 Valencia, Spain*
⁷⁵*University of Victoria, Victoria, British Columbia, Canada V8W 3P6*
⁷⁶*Department of Physics, University of Warwick, Coventry CV4 7AL, United Kingdom*
⁷⁷*University of Wisconsin, Madison, Wisconsin 53706, USA*

(Received 25 May 2011; published 5 July 2011)

We present branching fraction and CP asymmetry measurements as well as angular studies of $B \rightarrow \phi\phi K$ decays using 464×10^6 $B\bar{B}$ events collected by the $BABAR$ experiment. The branching fractions are measured in the $\phi\phi$ invariant mass range below the η_c resonance ($m_{\phi\phi} < 2.85$ GeV). We find $\mathcal{B}(B^+ \rightarrow \phi\phi K^+) = (5.6 \pm 0.5 \pm 0.3) \times 10^{-6}$ and $\mathcal{B}(B^0 \rightarrow \phi\phi K^0) = (4.5 \pm 0.8 \pm 0.3) \times 10^{-6}$, where the first uncertainty is statistical and the second systematic. The measured direct CP asymmetries for the B^\pm decays are $A_{CP} = -0.10 \pm 0.08 \pm 0.02$ below the η_c threshold ($m_{\phi\phi} < 2.85$ GeV) and $A_{CP} = 0.09 \pm 0.10 \pm 0.02$ in the η_c resonance region ($m_{\phi\phi}$ in $[2.94, 3.02]$ GeV). Angular distributions are consistent with $J^P = 0^-$ in the η_c resonance region and favor $J^P = 0^+$ below the η_c resonance.

DOI: [10.1103/PhysRevD.84.012001](https://doi.org/10.1103/PhysRevD.84.012001)

PACS numbers: 13.25.Hw, 14.40.Nd

*Now at Temple University, Philadelphia, PA 19122, USA

† Also with Università di Perugia, Dipartimento di Fisica, Perugia, Italy

‡ Now at the University of South Alabama, Mobile, AL 36688, USA

§ Also with Università di Sassari, Sassari, Italy

The violation of CP symmetry is a well-known requirement for the matter-antimatter imbalance of the Universe [1]. The *BABAR* [2] and Belle [3] experiments at the high-luminosity B factories, PEP-II [4] and KEKB [5], have made numerous CP asymmetry measurements using data sets 2 orders of magnitude larger than their predecessors. All of these measurements are consistent with a single source of CP violation—the complex phase within the Cabibbo-Kobayashi-Maskawa (CKM) quark mixing matrix of the standard model [6]. However, with the small amount of CP violation from the CKM matrix, it is difficult to explain the matter-antimatter asymmetry of the Universe [7]. This motivates searches for new sources of CP violation.

A method to search for new sources of CP -violating phases is to measure CP asymmetries in hadron decays that are forbidden at the tree level [8]. Since the leading decay amplitude is a one-loop process, contributions within the loop from virtual non-standard-model particles cannot be excluded. The quark interactions with the non-standard-model particles can introduce new CP violating phases in the decay amplitude, which can lead to observable nonzero CP asymmetries. Decays of B mesons with a $b \rightarrow s\bar{s}$ transition have been extensively studied for this reason.

The three-body $B \rightarrow \phi\phi K$ decay is a one-loop “penguin” $b \rightarrow s\bar{s}$ transition. This final state can also occur through the tree-level decay $B \rightarrow \eta_c K$, followed by $\eta_c \rightarrow \phi\phi$, where the B decay is a $b \rightarrow c\bar{c}s$ transition. If the $\phi\phi$ invariant mass $m_{\phi\phi}$ in the three-body $B \rightarrow \phi\phi K$ decay is close to the η_c resonance, the tree and penguin amplitudes may interfere. Within the standard model, the relative weak phase between these amplitudes is $\arg(V_{tb}V_{ts}^*/V_{cb}V_{cs}^*) \approx 0$, so no CP violation is expected from the interference. However, new physics contributions to the penguin loop in the $B \rightarrow \phi\phi K$ decay could introduce a nonzero relative CP violating phase, which may then produce a significant direct CP asymmetry [9]. Measurement of a significant, nonzero direct CP asymmetry would be an unambiguous sign of new physics. A previous measurement of the direct CP asymmetry [10] was consistent with zero, but was also limited by a large statistical uncertainty. The B^+ and B^0 branching fractions have been previously measured [10,11] to be a few times 10^{-6} . Theoretical predictions of the branching fractions are of the same order [12,13].

I. DATA SET AND DETECTOR DESCRIPTION

We present measurements of the $B^+ \rightarrow \phi\phi K^+$ and $B^0 \rightarrow \phi\phi K^0$ branching fractions [14] and direct CP asymmetry $A_{CP} \equiv [N(B^-) - N(B^+)]/[N(B^-) + N(B^+)]$ as well as studies of angular distributions performed using $464 \times 10^6 B\bar{B}$ pairs collected by the *BABAR* experiment at the SLAC National Accelerator Laboratory. The direct CP asymmetry is measured both below and within the η_c resonance region of the $\phi\phi$ invariant mass with these regions defined as $m_{\phi\phi} < 2.85$ GeV and $m_{\phi\phi}$ within

[2.94, 3.02] GeV, respectively [15]. The branching fractions are measured in the $m_{\phi\phi}$ region below the η_c resonance ($m_{\phi\phi} < 2.85$ GeV).

The *BABAR* detector is described in detail elsewhere [2]. What follows is a brief overview of the main features of the detector. The detector has a roughly cylindrical geometry, with the axis along the beam direction. The trajectories, momenta, and production vertices of charged particles are reconstructed from position measurements made by a silicon vertex tracker (SVT) and a 40-layer drift chamber (DCH). The SVT consists of 5 layers of double-sided silicon strip detectors which provide precision position measurements close to the beam interaction region. Both the SVT and DCH measure the specific energy loss (dE/dx) along the charged particle trajectory, which is used to infer the particle mass from the velocity dependence of the energy loss and the momentum measurement. The tracking system is inside a uniform 1.5 T magnetic field provided by a superconducting solenoid. Outside the tracking system lies the Detector of Internally Reflected Cherenkov radiation (DIRC), which is an array of quartz bars coupled with an array of phototubes which detect the Cherenkov light produced when a charged particle travels through the quartz bars. The measured Cherenkov angle is used to infer the particle mass from the velocity dependence of the Cherenkov angle and the measured momentum. The energies of photons and electrons are determined from the measured light produced in electromagnetic showers inside a CsI crystal calorimeter (EMC). The Instrumented Flux Return (IFR) uses resistive plate chambers and limited streamer tubes within the iron of the magnet flux return to identify muons and neutral hadrons.

We use Monte Carlo (MC) samples to determine the signal selection efficiency. The MC events are generated with EVTGEN [16] and simulated using GEANT4 [17].

II. EVENT SELECTION

We select events containing multiple hadrons by requiring at least three charged tracks in the event and the ratio of the second to zeroth Fox-Wolfram [18] moments R_2 to be less than 0.98.

Charged kaon candidates are required to pass a selection based on a likelihood ratio which uses the SVT and DCH dE/dx and the DIRC Cherenkov angle measurements as inputs to the likelihood. The ratio is defined as $R_{hh'} \equiv \mathcal{L}_h/(\mathcal{L}_h + \mathcal{L}_{h'})$, where h and h' are K , π , or p . The minimum kaon selection criterion is $R_{K\pi} > 0.2$ or $R_{p\pi} > 0.2$. This selection has an efficiency greater than 98% for kaons and a pion efficiency of less than 15% below a lab momentum of 2.5 GeV. Candidate $\phi \rightarrow K^+K^-$ decays are constructed from oppositely-charged kaon candidates with an invariant mass in the range of 0.987 to 1.2 GeV. At least one of the kaons in each $\phi \rightarrow K^+K^-$ candidate must also satisfy the more stringent criteria of $R_{K\pi} > 0.8176$ and $R_{Kp} > 0.018$, which has an efficiency

greater than 90% for kaons and a pion efficiency of less than 3% below a lab momentum of 2.5 GeV.

Candidate $K_S^0 \rightarrow \pi^+ \pi^-$ decays are constructed from oppositely-charged pion candidates with an invariant mass in the range of 0.486 to 0.510 GeV. The pion tracks are fit to a common vertex. The χ^2 probability of the vertex fit must be greater than 0.001. The typical experimental resolution on the measured K_S^0 flight length in the plane transverse to the beam is around 0.2 mm or less. We require the transverse flight length to be at least 2 mm.

Candidate $B \rightarrow \phi \phi K$ decays are constructed from pairs of ϕ candidates that do not share any daughters and either a K^\pm or a K_S^0 candidate. The ϕ and K^\pm candidates are constrained to a common vertex. We reject combinatoric background by requiring the B candidate to have kinematics consistent with $Y(4S) \rightarrow B\bar{B}$ using two standard variables: m_{ES} and ΔE . The energy-substituted B mass is defined as $m_{ES} \equiv \sqrt{E_{\text{beam}}^{*2} - p^{*2}}$, where E_{beam}^* and p^* are the beam energy ($\sqrt{s}/2$) and the reconstructed B momentum, both in the center-of-mass (CM) reference frame. The energy difference is defined as $\Delta E \equiv E^* - E_{\text{beam}}^*$, where E^* is the reconstructed B energy in the CM frame. We require m_{ES} and ΔE to be within [5.20, 5.29] GeV and [-0.1, 0.1] GeV, respectively. The experimental resolution is about 2.7 MeV for m_{ES} and 15 MeV for ΔE .

The m_{ES} interval includes a large ‘‘sideband’’ region below the area where the signal is concentrated near the B mass. The ΔE interval also is wide enough to include sideband regions where the signal probability is very low. Including events in the sideband regions enables us to determine the probability density functions (PDFs) of the combinatoric background directly in the maximum likelihood (ML) fits of the data.

About 7% of events in signal Monte Carlo samples have more than one $B \rightarrow \phi \phi K$ candidate. If there are multiple $B^+ \rightarrow \phi \phi K^+$ candidates in a single event, we select the B^+ candidate with the smallest mass χ_m^2 defined as $\sum_i \frac{(m_i - m_0)^2}{\sigma^2}$, where the sum i is over the two ϕ candidates, m_i (m_0) is the reconstructed (nominal) ϕ mass, and σ is the RMS of the reconstructed m_ϕ distribution for properly reconstructed ϕ candidates. If there are more than one B^+ candidates that use the same two ϕ candidates, we choose the B^+ candidate with the highest quality K^+ identification for the K^+ from the B^+ decay. If the quality level of the K^+ identification is the same for these B^+ candidates, we choose the B^+ candidate with the highest vertex χ^2 probability. For events with multiple $B^0 \rightarrow \phi \phi K_S^0$, the sum for χ_m^2 includes the $K_S^0 \rightarrow \pi^+ \pi^-$, and we choose the B^0 with the smallest χ_m^2 . For both the B^+ and B^0 decay modes, the probability that the algorithms described above choose the correct candidate is about 87%.

The reconstruction and selection efficiencies for events with $m_{\phi\phi} < 2.85$ GeV are determined from Monte Carlo

samples to be 28.0% and 22.5% for the B^+ and B^0 modes, respectively.

We use control samples of $B \rightarrow D_s D$ decays where $D_s \rightarrow \phi \pi$, $D \rightarrow K \pi$, and $\phi \rightarrow K^+ K^-$ to determine corrections to the $B \rightarrow \phi \phi K$ signal probability density function parameters determined from Monte Carlo samples in the maximum likelihood fits described below.

A. Continuum background

The events that pass the selection above with at least one B candidate are primarily background events from the continuum ($e^+ e^- \rightarrow q\bar{q}$ with $q = u, d, s, c$). We reduce this background by using a Fisher discriminant (\mathcal{F}), which is the linear combination of seven variables and is optimized for maximum separation power of signal and the continuum background. The seven variables are listed below. These variables are commonly used by the *BABAR* experiment in analyses of charmless B decays, where the primary background is from continuum events. They take advantage of aspects of the production distributions and event topologies of $B\bar{B}$ versus continuum $q\bar{q}$ production events.

- (i) $|\Delta t / \sigma_{\Delta t}|$: the absolute value of the reconstructed proper time difference between the two B decays divided by its uncertainty [19].
- (ii) $|FT|$: the absolute value of the standard *BABAR* flavor tagging neural network output [19].
- (iii) $|\cos\theta_{\text{th}}^*|$: the absolute value of the cosine of the angle between the B candidate thrust axis and the thrust axis of the rest of the event computed in the CM frame. The thrust axis is the direction that maximizes the scalar sum of the projection of the track momenta on that direction.
- (iv) $|\cos\theta_{\text{Bthr}}^*|$: the absolute value of the cosine between the thrust axis of the B candidate and the beam axis in the CM frame. Signal events have a uniform distribution in this variable, while continuum background follows a $|1 + \cos^2\theta|$ distribution, where θ is the angle between the thrust direction and the beam axis.
- (v) $|\cos\theta_B^*|$: the absolute value of the cosine of the angle between the B direction and the beam axis in the CM frame. The angular distribution of the signal follows a $\sin^2\theta_B^*$ distribution, while the continuum background is uniformly distributed.
- (vi) L_0 and L_2 : The zeroth and second angular moments of the momentum flow of the rest of the event about the B thrust axis, defined as $L_j \equiv \sum_i p_i |\cos\theta_i|^j$, where the angle θ_i is the angle between track i and the B thrust axis and the sum excludes the daughters of the B candidate. The calculations are done in the CM frame.

Distributions of \mathcal{F} for signal and continuum MC samples are shown in Fig. 1. The Fisher discriminant \mathcal{F} is used as

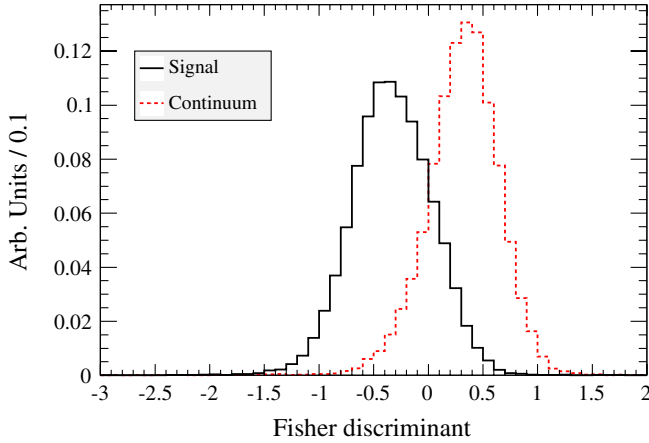


FIG. 1 (color online). Distributions of the Fisher discriminant \mathcal{F} for $B \rightarrow \phi\phi K$ signal (solid black) and $e^+e^- \rightarrow q\bar{q}$ continuum (dashed red) Monte Carlo simulation.

one of several variables in the maximum likelihood fits described below.

B. Peaking backgrounds

The ultimate detected state of our $B \rightarrow \phi\phi K$ signal decay is five kaons. In addition to the ϕ resonance, there may be contributions to each K^+K^- pair either from other intermediate K^+K^- resonances, such as the $f_0(980)$, or from nonresonant K^+K^- contributions. We use the K^+K^- mass sidebands for each ϕ candidate to determine the amount of B mesons that decay to the detected five-kaon state (which we denote $B \rightarrow 5K$) that are not coming from $B \rightarrow \phi\phi K$. The specific B decays that we consider as backgrounds are $B \rightarrow \phi K^+K^-K$, $B \rightarrow K^+K^-K^+K^-K$, $B \rightarrow f_0\phi K$, and $B \rightarrow f_0K^+K^-K$. The branching fractions for these decays are currently unknown. We call these B decays “peaking backgrounds” because properly reconstructed B candidates are indistinguishable from our $B \rightarrow \phi\phi K$ signal in the m_{ES} , ΔE , and \mathcal{F} variables.

We perform unbinned extended maximum likelihood fits to determine the signal and combinatoric background yields and, in some cases, the charge asymmetry. All of the fits use the product of one-dimensional PDFs of m_{ES} , ΔE , and \mathcal{F} in the likelihood. For the $B \rightarrow \phi\phi K$ branching fraction measurements, we also include PDFs for the invariant mass of each $\phi \rightarrow K^+K^-$ candidate ($m_{\phi 1}$ and $m_{\phi 2}$).

As a first step, we divide the $m_{\phi 1}$ vs $m_{\phi 2}$ plane [20] in the range of 0.987 to 1.200 GeV into five mutually exclusive zones. We fit for the $B \rightarrow 5K$ yield in each zone using only m_{ES} , ΔE , and \mathcal{F} in the likelihood. The zones are based on various combinations of the ϕ signal and sideband regions, which are defined as LOW-SB [0.987, 1.000] GeV, PHI-SIGNAL [1.00, 1.04] GeV, and HIGH-SB [1.04, 1.20] GeV. Each of the five zones is chosen so that either the $B \rightarrow \phi\phi K$ signal or one of the four peaking B

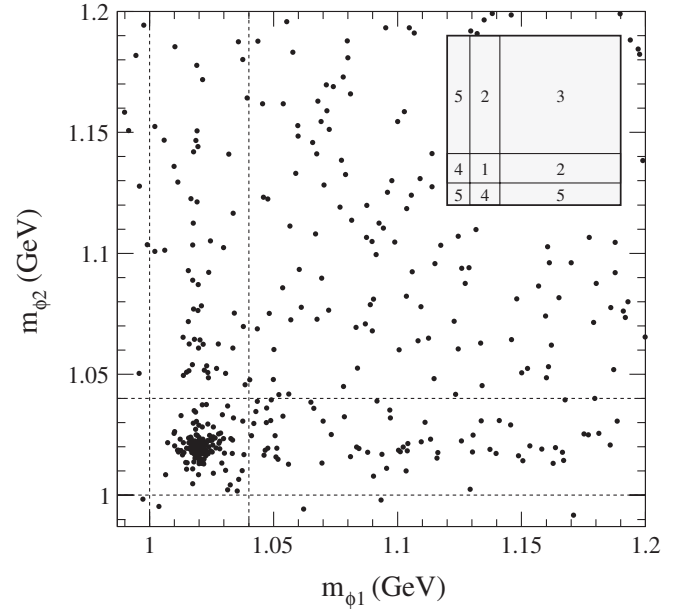


FIG. 2. Data distribution of $B^+ \rightarrow 5K$ events in the $m_{\phi 2}$ vs $m_{\phi 1}$ plane for events with $m_{\phi\phi} < 2.85$ GeV. To enhance the $B \rightarrow 5K$ signal for the figure, we have required $m_{ES} > 5.27$ GeV, $|\Delta E| < 0.040$ GeV, and $\mathcal{F} < 0.0$. The efficiency of these additional requirements, relative to the nominal selection, is about 70% for the signal. The inset shows the definition of the five zones.

backgrounds is concentrated in the region. We compute the number of peaking background events within the m_{ϕ} range used for the branching fraction fit by using the results of the five zone fits as described below.

Figure 2 shows the distribution of events in the $m_{\phi 2}$ vs $m_{\phi 1}$ plane for the selected $B^+ \rightarrow 5K$ candidates in the data. To enhance the $B^+ \rightarrow 5K$ signal for the figure, we have required $m_{ES} > 5.27$ GeV, $|\Delta E| < 0.040$ GeV, and $\mathcal{F} < 0.0$. The inset of the figure shows the definition of the five zones. A concentration of events in the PHI-SIGNAL region for both ϕ candidates (zone 1) is clearly evident. The region defined as PHI-SIGNAL combined with HIGH-SB for either ϕ candidate (zone 2) contains the largest fraction of the $B \rightarrow \phi K^+K^-K$ mode, although the $B \rightarrow \phi\phi K$ signal also populates this region due to cases where one ϕ is misreconstructed. The zone where the invariant mass of both ϕ candidates is in the HIGH-SB region (zone 3) contains the largest concentration of the nonresonant $B \rightarrow K^+K^-K^+K^-K$ mode. Zones 4 and 5 contain a large fraction of the $B \rightarrow f_0\phi K$ and $B \rightarrow f_0K^+K^-K$ modes, respectively, and very small fractions of the other three modes.

Monte Carlo samples for the five B decay modes (signal plus four peaking background modes) are used to determine the fraction of events in each zone (i) for each decay mode (j), which we denote with the matrix f_{ij} . The total $B \rightarrow 5K$ yield (n_i) is determined for each zone i using five

separate maximum likelihood fits of the data. The yield for each B decay mode (N_j) and the amount of each mode j in zone i (n_{ij}) can be determined from

$$N_j = \sum_i f_{ij}^{-1} n_i \quad \text{and} \quad n_{ij} = f_{ij} N_j. \quad (1)$$

Zone 1 corresponds to the m_ϕ range used in the branching fraction maximum likelihood fit.

C. Maximum likelihood fits

The extended maximum likelihood fits in the five zones determine the $B \rightarrow 5K$ signal and combinatoric background yields in each zone. The $B \rightarrow 5K$ signal is split into properly reconstructed and misreconstructed (“self-crossfeed”) components, with the self-crossfeed fraction fixed. The self-crossfeed component is defined as events where a true $B \rightarrow 5K$ decay is present in the event, but one or more tracks used in the reconstructed B are either from the other B in the event or not real. In zone 1, the self-crossfeed fraction for $B \rightarrow \phi\phi K$ decays is around 7%.

The properly reconstructed $B \rightarrow 5K$ signal component is described by the following PDFs: a Crystal Ball function [21] for m_{ES} , the sum of three Gaussians for ΔE , and the sum of a bifurcated Gaussian and a Gaussian for \mathcal{F} . The Crystal Ball function is a Gaussian modified to have an extended power-law tail on the low side. The $B \rightarrow 5K$ signal PDF parameters are determined from MC samples with corrections to the m_{ES} and ΔE core mean and width parameters from the $B \rightarrow D_s D$ control samples. The mean corrections are 0.04 ± 0.11 MeV and -3.5 ± 0.8 MeV for m_{ES} and ΔE , respectively. The width scale factors are 1.10 ± 0.04 and 1.04 ± 0.05 for m_{ES} and ΔE , respectively. The combinatoric background is described by the following PDFs: an empirical threshold function [22] for m_{ES} , a first-order polynomial for ΔE , and the sum of two Gaussians for \mathcal{F} . Most of the combinatoric background PDF shape parameters are determined in the fits.

The results of the five zone fits for the B^+ and B^0 modes are given in Tables V and VI, respectively, in the Appendix. The $B \rightarrow \phi\phi K$ signal is observed in both the B^+ and B^0 samples. The $B^0 \rightarrow \phi\phi K^0$ decay has not been observed previously. The B yield in zone 2 for the B^+ mode is significant, but about half of this is due to misreconstructed $B \rightarrow \phi\phi K$ signal. The computed $B^+ \rightarrow \phi K^+ K^- K^+$ and $B^+ \rightarrow K^+ K^- K^+ K^- K^+$ yields are positive, but the significance is less than 2 standard deviations. There is no evidence of either $B \rightarrow f_0 \phi K$ or $B \rightarrow f_0 K^+ K^- K$. The branching fraction maximum likelihood fits use the m_ϕ range that corresponds to zone 1. We fix the yield of each of the four peaking background modes to the zone 1 value in Table V or VI for the branching fraction fit described below.

III. BRANCHING FRACTION ANALYSIS

The maximum likelihood fit used to measure the $B \rightarrow \phi\phi K$ yield below the η_c resonance for the branching fraction measurement restricts the event selection with $m_{\phi\phi} < 2.85$ GeV and m_ϕ within [1.00, 1.04] GeV, which corresponds to zone 1 in the peaking background discussion above. The fit components are $B \rightarrow \phi\phi K$ signal, combinatoric background, and the four peaking backgrounds.

In addition to m_{ES} , ΔE , and \mathcal{F} , PDFs for $m_{\phi 1}$ and $m_{\phi 2}$ are included in the likelihood function. For each fit component, each ϕ candidate has a PDF that is the sum of a properly reconstructed $\phi \rightarrow K^+ K^-$ decay, given by a relativistic Breit-Wigner function, and a misreconstructed ϕ , described by a first-order polynomial. The $m_{\phi 1}$ and $m_{\phi 2}$ PDFs are combined in a way that is symmetric under $1 \leftrightarrow 2$ exchange and takes into account the fractions of events where both ϕ candidates are properly reconstructed, one ϕ is misreconstructed, and both ϕ candidates are misreconstructed.

In addition to the signal and combinatoric background yields, the charge asymmetry for the signal and combinatoric background components and most of the combinatoric background PDF parameters are determined in the fit.

The results of the B^+ and B^0 fits are shown in Figs. 3 and 4, respectively. To reduce the combinatoric background in each distribution shown in the figures, a requirement is made on a likelihood ratio, which is based on all the fit variables except the one plotted.

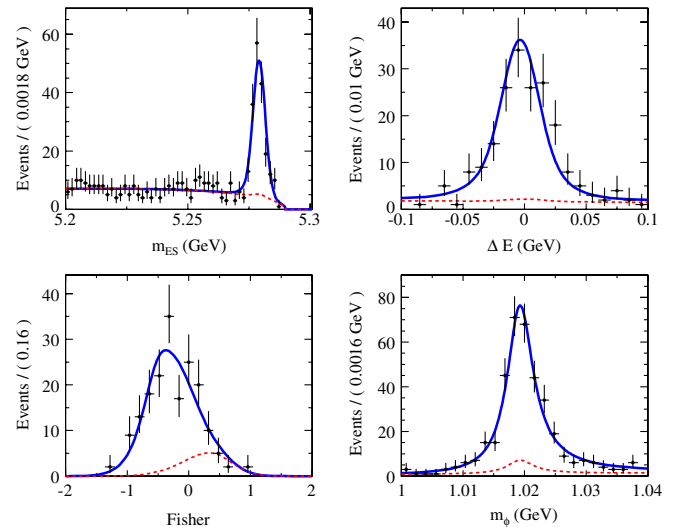


FIG. 3 (color online). Results of fitting the $B^+ \rightarrow \phi\phi K^+$ sample for $m_{\phi\phi} < 2.85$ GeV. The dashed red curve is the sum of the combinatoric and peaking background components. The solid blue curve is for all components. A requirement on a likelihood ratio based on all fit variables except the one plotted is made to reject most of the background. The likelihood ratio requirements are about 84% efficient for the signal.

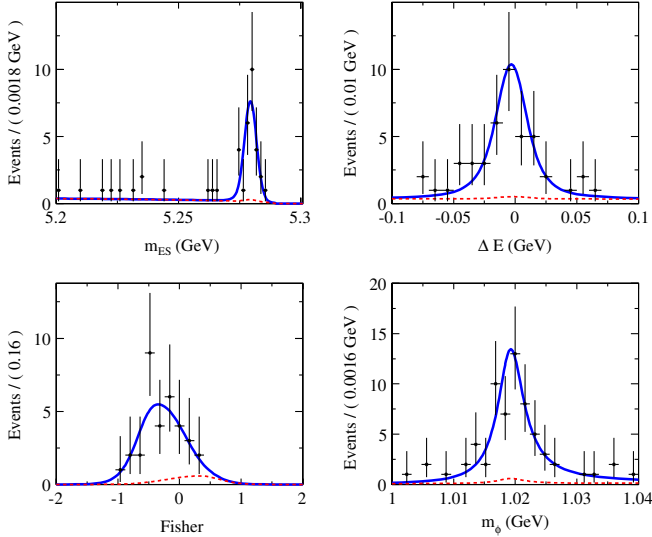


FIG. 4 (color online). Results of fitting the $B^0 \rightarrow \phi\phi K_S^0$ sample for $m_{\phi\phi} < 2.85$ GeV. The dashed red curve is the sum of the combinatoric and peaking background components. The solid blue curve is for all components. A requirement on a likelihood ratio based on all fit variables except the one plotted is made to reject most of the background. The likelihood ratio requirements are about 84% efficient for the signal.

The fitted charge asymmetry \mathcal{A}_{CP} for the background component is 0.02 ± 0.03 . The charge asymmetry for the signal component is -0.10 ± 0.08 . The fitted yields of B^+ and B^0 signal candidates with $m_{\phi\phi} < 2.85$ GeV are 178 ± 15 events and 40 ± 7 events, respectively, where the uncertainties are statistical only.

A. Systematic uncertainties

Table I summarizes the systematic uncertainties on the $B \rightarrow \phi\phi K$ branching fractions in the $m_{\phi\phi} < 2.85$ GeV region. The systematics are divided into additive uncertainties that affect the B yield measurement and multiplicative uncertainties in the branching fraction calculation.

The uncertainties from the corrections applied to the PDF parameters such as the m_{ES} and ΔE core mean and width for the signal component, which are derived from data control samples, are listed under ‘‘ML fit yield.’’ The signal Fisher and m_ϕ core Gaussian mean and width parameters are not corrected in the fit, because data control sample measurements are consistent with the Monte Carlo. However, we did vary the signal Fisher and m_ϕ core Gaussian mean and width parameters by the statistical uncertainty of the data control sample measurements. These variations are also included under ‘‘ML fit yield.’’ The fit bias systematic is taken to be half of the bias correction added in quadrature with the statistical uncertainty on the bias. We vary the fixed peaking background yields by their statistical uncertainties (see Tables V and VI) and by varying the fractions f_{ij} . The fixed self-

TABLE I. Summary of the systematic and statistical uncertainties for the branching fraction measurements.

Quantity	$B^+ \rightarrow \phi\phi K^+$	$B^0 \rightarrow \phi\phi K^0$
Fit stat. uncertainty (events)	15.1	7.0
Additive uncertainties (events)		
ML fit yield	3.3	1.0
ML fit bias	1.6	0.2
Peaking BG, region fits	3.5	1.2
Peaking BG, f_{ij} values	3.0	0.8
Self-crossfeed fraction	1.8	0.4
Total additive syst. (events)	6.2	1.8
Multiplicative uncertainties (%)		
Tracking efficiency	1.2	1.0
K_S^0 Reconstruction efficiency	...	1.5
Number $B\bar{B}$	1.1	1.1
$\mathcal{B}(\phi \rightarrow K^+ K^-)$	1.2	1.2
$\mathcal{B}(K_S^0 \rightarrow \pi^+ \pi^-)$...	0.1
MC statistics	0.1	0.1
$m_{\phi\phi}$ Cut efficiency	0.2	0.3
K^\pm identification	3.0	2.0
Total multiplicative syst. (%)	3.6	3.2
Total systematic [\mathcal{B}] ($\times 10^{-6}$)	0.3	0.3
Statistical [\mathcal{B}] ($\times 10^{-6}$)	0.5	0.8

crossfeed fraction for the signal component was varied by $\pm 2\%$. Adding the individual uncertainties in quadrature, the total additive systematic uncertainties on the B^+ and B^0 signal yields are 6.2 and 1.8 events, respectively.

The uncertainty on the track reconstruction efficiency is $\pm 0.23\%$ per track, which is taken to be fully correlated for the charged kaons. The K_S^0 reconstruction efficiency has an uncertainty of 1.5%. The $\phi \rightarrow K^+ K^-$ and $K_S^0 \rightarrow \pi^+ \pi^-$ branching fractions are taken from the PDG [23] and are varied by their 1 standard deviation uncertainties. The systematic uncertainty on the K^\pm identification criteria was estimated by comparing the ratio of the B yield with the nominal selection to the B yield requiring all K^\pm to pass the tighter selection in the data and the MC samples. This gives an uncertainty of 3% for the B^+ mode and 2% for the B^0 mode. Adding the individual uncertainties in quadrature, the overall multiplicative systematic uncertainties are 3.6% for the B^+ mode and 3.2% for the B^0 mode.

The signal charge asymmetry has been corrected for a bias due to differences in the K^+ and K^- efficiencies by adding $+0.010 \pm 0.005$ to the asymmetry. The overall 2% systematic uncertainty takes into account uncertainties on the charge dependence of the tracking efficiency, material interaction cross section for kaons, and particle identification.

B. Branching fraction results

Table II summarizes the $B \rightarrow \phi\phi K$ branching fraction results for $m_{\phi\phi} < 2.85$ GeV. We find

TABLE II. Branching fraction and charge asymmetry results for $B \rightarrow \phi\phi K$ in the region $m_{\phi\phi} < 2.85$ GeV. The statistical significance is given by $\sqrt{2\ln(\mathcal{L}_{\max}/\mathcal{L}_0)}$, where \mathcal{L}_{\max} is the maximum likelihood and \mathcal{L}_0 is the likelihood for the hypothesis of no $\phi\phi K$ signal. The significance does not include systematic uncertainties.

	$B^+ \rightarrow \phi\phi K^+$	$B^0 \rightarrow \phi\phi K^0$
Events to fit	1535	293
Fit signal yield	178 ± 15	40 ± 7
ML fit bias (events)	3.0 ± 0.5	0.0 ± 0.2
MC efficiency (%)	28.0	22.5
$\Pi \mathcal{B}_i$ (%)	24.2	8.4
Stat. significance	24	11
$\mathcal{B}(10^{-6})$	$5.6 \pm 0.5 \pm 0.3$	$4.5 \pm 0.8 \pm 0.3$
Signal A_{CP}	$-0.10 \pm 0.08 \pm 0.02$...
Comb. bkg. A_{CP}	0.02 ± 0.03	...

$$\begin{aligned} \mathcal{B}(B^+ \rightarrow \phi\phi K^+) &= (5.6 \pm 0.5 \pm 0.3) \times 10^{-6} \\ \mathcal{B}(B^0 \rightarrow \phi\phi K^0) &= (4.5 \pm 0.8 \pm 0.3) \times 10^{-6}, \end{aligned} \quad (2)$$

where the first uncertainty is statistical and the second systematic. These results are consistent with and supersede the previous measurements [11] by the *BABAR* Collaboration. The Belle collaboration measurements [10] are lower, though they are statistically compatible. Our branching fraction measurements are higher than the theoretical predictions of [12,13].

IV. CP ASYMMETRY IN η_c RESONANCE REGION

As was mentioned in the introduction, a significant non-zero direct CP asymmetry in the η_c resonance region of $m_{\phi\phi}$ would be a clear sign of physics beyond the standard model. For this measurement, we use the simpler likelihood, based on m_{ES} , ΔE , and \mathcal{F} . Figure 5 shows the fitted $B^+ \rightarrow \phi\phi K^+$ yield as a function of $m_{\phi\phi}$. The η_c resonance is clearly visible. Narrow bins around the χ_{c0} and χ_{c2} resonances do not show a significant excess above the broad nonresonant component.

The results of fitting the events in the $m_{\phi\phi}$ range of [2.94, 3.02] GeV are given in Table III. For the CP asymmetry, we find

$$A_{CP}(m_{\phi\phi} \text{ in } [2.94, 3.02] \text{ GeV}) = -0.09 \pm 0.10 \pm 0.02,$$

where the first uncertainty is statistical and the second uncertainty is systematic. The value above includes the same 1% bias correction and has the same 2% overall systematic uncertainty as the signal charge asymmetry below the η_c resonance as described above.

The fit yields 100 ± 10 signal candidates. Using $\mathcal{B}(B^+ \rightarrow \eta_c K^+) = (9.1 \pm 1.3) \times 10^{-4}$ and $\mathcal{B}(\eta_c \rightarrow \phi\phi) = (2.7 \pm 0.9) \times 10^{-3}$ from the PDG [23], a $B^+ \rightarrow \phi\phi K^+$; $\phi \rightarrow K^+ K^-$ reconstruction efficiency of 29% in

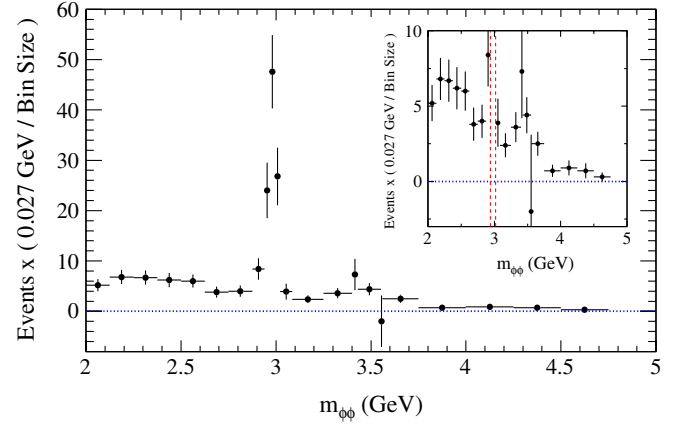


FIG. 5 (color online). Fitted $B^+ \rightarrow \phi\phi K^+$ yield as a function of $m_{\phi\phi}$. Each point shows the results of a maximum likelihood fit of the events in that bin. The inset is the same data with an expanded vertical range to show the shape of the nonresonant component more clearly. The yield has been divided by the bin width and scaled by 0.027 GeV, which is the bin width of the three bins in the η_c resonance region ([2.94, 3.02] GeV and dashed vertical lines in the inset). The two narrow bins above the η_c are centered on the χ_{c0} (bin range [3.400, 3.430] GeV) and the χ_{c2} (bin range [3.552, 3.560] GeV).

the η_c resonance region, and an efficiency of 78% for the $m_{\phi\phi}$ window of [2.94, 3.02] GeV for the η_c resonance, we would expect 62 ± 22 signal events, ignoring the nonresonant $B^+ \rightarrow \phi\phi K^+$ contribution and any interference between the resonant η_c and nonresonant amplitudes. We do not use our B^+ event yield to measure $\mathcal{B}(B^+ \rightarrow \eta_c K^+) \times \mathcal{B}(\eta_c \rightarrow \phi\phi)$ due to the potentially large interference effects between the resonant and nonresonant $\phi\phi$ amplitudes which we can not easily quantify.

The A_{CP} may integrate to zero, even if there is a contributing non-standard-model amplitude with a nonzero CP violating phase. However, in this case the phase variation of the η_c resonance amplitude could give nonzero A_{CP} values with opposite signs above and below the peak of the resonance. We have performed the measurement in two ranges, splitting the η_c region into two regions (above and below the peak of the resonance). The results are

TABLE III. Fit results for $B^+ \rightarrow \phi\phi K^+$ within η_c resonance region ($m_{\phi\phi}$ within [2.94, 3.02] GeV). The signal charge asymmetry A_{CP} has been corrected by adding $+0.010 \pm 0.005$ to the fitted asymmetry.

ML fit quantity/analysis	$B^+ \rightarrow \phi\phi K^+$
Events to fit	181
Fit signal yield	100 ± 10
MC efficiency (%)	29.2
Corr. signal A_{CP}	$-0.09 \pm 0.10 \pm 0.02$
Comb. bkg. A_{CP}	-0.06 ± 0.11

$$A_{CP}(m_{\phi\phi} \text{ in}[2.94, 2.98] \text{ GeV}) = -0.10 \pm 0.15 \pm 0.02$$

$$A_{CP}(m_{\phi\phi} \text{ in}[2.98, 3.02] \text{ GeV}) = -0.08 \pm 0.14 \pm 0.02,$$

both of which are consistent with zero, as expected in the standard model.

V. ANGULAR STUDIES

We use the angular variables that describe the $B^+ \rightarrow \phi\phi K^+$ decay to investigate the spin components of the $\phi\phi$ system below and within the η_c resonance. The angles are defined as follows.

- (i) θ_i , ($i = 1, 2$): The θ_i angle is the angle between the momentum of the K^+ coming from the decay of ϕ_i in the ϕ_i rest frame with respect to the boost direction from the $\phi\phi$ rest frame to the ϕ_i rest frame.
- (ii) χ : The χ angle is the dihedral angle between the ϕ_1 and ϕ_2 decay planes in the $\phi\phi$ rest frame.
- (iii) $\theta_{\phi\phi}$: The $\theta_{\phi\phi}$ angle is the angle between one of the ϕ mesons in $\phi\phi$ rest frame with respect to the boost direction from the B^+ rest frame to the $\phi\phi$ rest frame.

We project the $J^P = 0^-$ component by making a histogram of $m_{\phi\phi}$ weighting each event by

$$P_2(\cos\theta_1)\text{Re}[Y_2^2(\theta_2, \chi)] = \frac{25}{4}\{3\cos^2\theta_1 - 1\}\sin^2\theta_2 \cos 2\chi,$$

where P_2 is a second-degree Legendre polynomial and Y_2^2 is a spherical harmonic with $\ell = 2$ and $m = 2$. In each bin, the $J^P = 0^-$ component yield is projected out, while the combinatoric background averages to zero. To do this, we select events in a signal region defined by: $m_{ES} > 5.27$ GeV, $|\Delta E| < 40$ MeV, m_ϕ within [1.01, 1.03] GeV, and $\mathcal{F} < 0.5$. The efficiency of these requirements, relative to the selection used in the asymmetry measurement, is about 78% for signal events and 2.9% for combinatoric background. The combinatoric background that remains after this selection is shown using data events in the

TABLE IV. Quality of the angular fits shown in Fig. 7. The first column is the $m_{\phi\phi}$ interval for the events in the fit. The last column is the p value of the χ^2 goodness-of-fit test for the hypothesis indicated in the third column.

$m_{\phi\phi}$ (GeV)	Variable	PDF	χ^2/N_{dof}	χ^2 prob.
[2.94, 3.02]	χ	$\sin^2\chi$	9.51/9	0.39
[2.94, 3.02]	χ	Uniform	60.3/9	1.2×10^{-9}
<2.85	χ	$\sin^2\chi$	41.6/9	3.9×10^{-6}
<2.85	χ	Uniform	18.5/9	0.030
[2.94, 3.02]	$\cos\theta$	$\sin^2\chi$	9.97/9	0.39
[2.94, 3.02]	$\cos\theta$	Uniform	60.5/9	1.1×10^{-9}
<2.85	$\cos\theta$	$\sin^2\chi$	32.9/9	1.7×10^{-4}
<2.85	$\cos\theta$	Uniform	25.8/9	2.2×10^{-3}
[2.94, 3.02]	$ \cos\theta_{\phi\phi} $	Uniform	9.02/9	0.44
<2.85	$ \cos\theta_{\phi\phi} $	Uniform	5.01/9	0.83

sideband region ($m_{ES} < 5.27$ GeV and $|\Delta E| < 100$ MeV) scaled by 0.065, which is the signal-to-sideband ratio for the combinatoric background.

The results are shown in Fig. 6. The weighted yield in the η_c region is consistent with all of the $B^+ \rightarrow \phi\phi K^+$ events having $J^P = 0^-$. Just below the η_c region, the weighted yield is consistent with zero. The excess in the bins near 2.2 GeV may be due to the $\eta(2225)$ seen in $J/\psi \rightarrow \gamma\phi\phi$ events at Mark III [24] and BES [25].

Figure 7 shows the background-subtracted distributions of χ , $\cos\theta_i$, and $|\cos\theta_{\phi\phi}|$ for the nominal event selection. The background subtraction is done with the technique described in Ref. [26]. Since there is no meaningful distinction between ϕ_1 and ϕ_2 , we combine the $\cos\theta_1$ and $\cos\theta_2$ distributions into one plot of $\cos\theta$. The reconstruction and selection efficiency, determined from MC

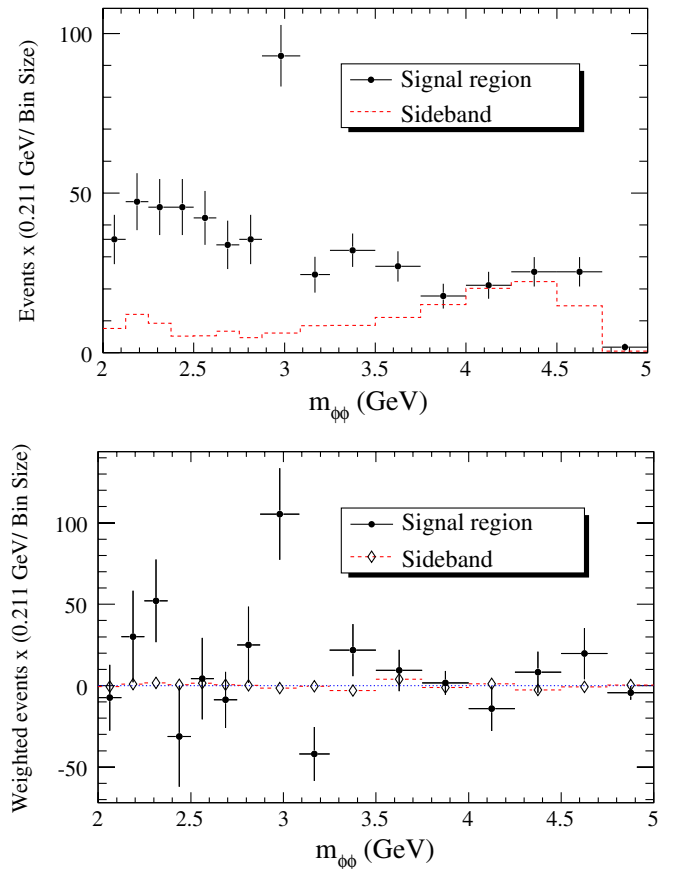


FIG. 6 (color online). Histograms (top) and weighted distributions (bottom) of $m_{\phi\phi}$ for the signal region (solid points) and data sideband selection (dashed with open diamonds) defined in the text. The sideband distributions have been normalized to the expected level of combinatoric background remaining after the signal region selection. Events in the bottom distribution were weighted by $P_2(\cos\theta_1)\text{Re}[Y_2^2(\theta_2, \chi)]$ which projects out the $J^P = 0^-$ component. The yield has been divided by the bin width and scaled by 0.211 GeV, which is the width of the bin covering the η_c resonance ([2.875, 3.086] GeV).

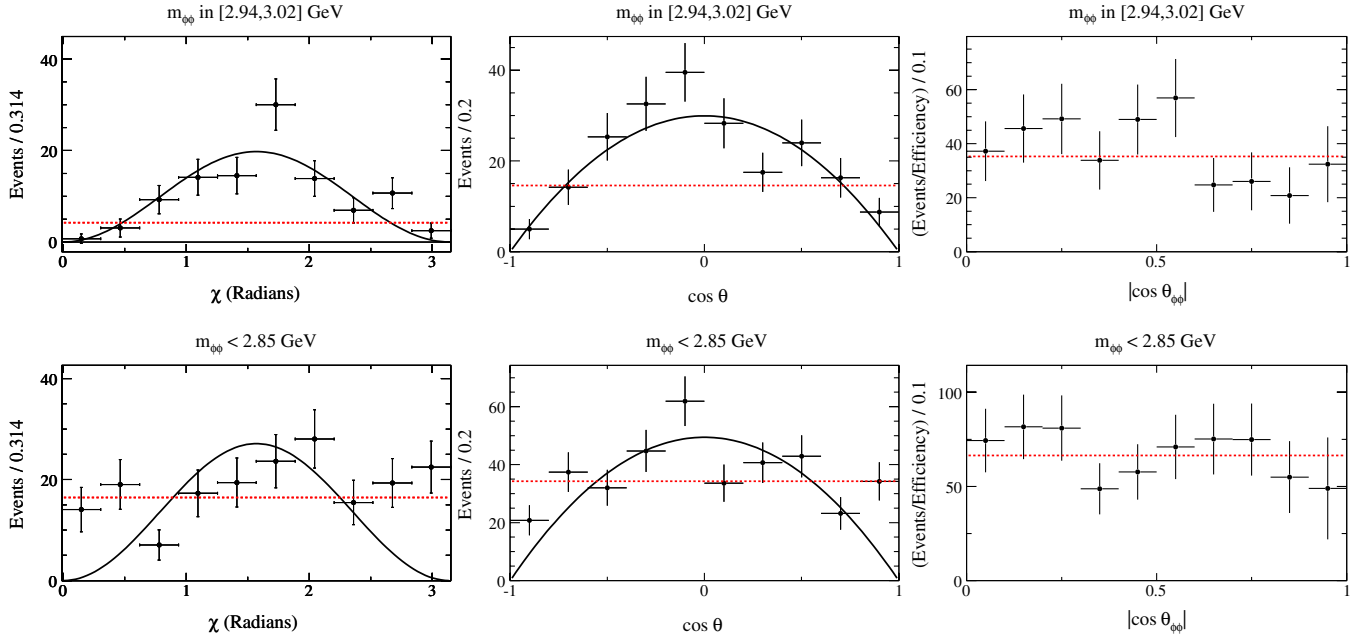


FIG. 7 (color online). Background-subtracted angular distributions in the η_c resonance region ($m_{\phi\phi}$ in [2.94, 3.02] GeV for the top row) and below the η_c resonance ($m_{\phi\phi} < 2.85$ GeV for the bottom row). The reconstruction and selection efficiency is uniform in χ (left) and $\cos\theta$ (center), but dependent on $|\cos\theta_{\phi\phi}|$ (right), so the right column has been efficiency corrected. The red dashed line shows a least- χ^2 fit of the points to a uniform distribution while the solid black curve shows a fit to the expectation for a $J^P = 0^-$ state decaying to $\phi\phi$. The fit χ^2/N_{dof} and χ^2 probabilities are given in Table IV.

samples, is uniform in χ and $\cos\theta_1$, but not in $|\cos\theta_{\phi\phi}|$, so the $|\cos\theta_{\phi\phi}|$ distribution is efficiency corrected. For each distribution, we performed a simple least- χ^2 fit to the distributions expected for both $J^P = 0^-$ and $J^P = 0^+$ for the $\phi\phi$ system. The fit χ^2/N_{dof} and χ^2 probabilities are given in Table IV.

For a $J^P = 0^-$ state, we expect χ to have a $\sin^2\chi$ distribution, while χ should be uniform for $J^P = 0^+$. The signal events in the η_c resonance region are consistent with a $\sin^2\chi$ distribution while the signal below the η_c resonance is not. For a $J^P = 0^-$ state, the distributions of $\cos\theta_i$ are expected to have $\sin^2\theta_i$ distributions, while a $J^P = 0^+$ state is expected to have uniform $\cos\theta_i$ distributions. The events in the η_c resonance region are consistent with a $\sin^2\theta_i$ distribution, while the events below the η_c resonance show a deviation from a $\sin^2\theta_i$ shape.

Finally, a spin-zero state should have a uniform $|\cos\theta_{\phi\phi}|$ distribution. The efficiency corrected distributions shown in Fig. 7, both within and below the η_c resonance region, are consistent with a uniform $|\cos\theta_{\phi\phi}|$ distribution.

VI. SUMMARY AND CONCLUSIONS

We have measured the branching fractions and charge asymmetries of $B \rightarrow \phi\phi K$ decays below the η_c resonance in the $\phi\phi$ invariant mass ($m_{\phi\phi} < 2.85$ GeV). We observe both $B^+ \rightarrow \phi\phi K^+$ and $B^0 \rightarrow \phi\phi K_S^0$, each with a significance of greater than 5 standard deviations. The

$B^0 \rightarrow \phi\phi K_S^0$ decay has not been observed previously. Our branching fraction measurements are higher than the theoretical predictions of [12,13].

We have measured the charge asymmetry for $B^+ \rightarrow \phi\phi K^+$ in the η_c resonance region, where a significant nonzero value would be an unambiguous indication of new physics. Our measurement is consistent with zero, which is the expectation of the standard model.

Finally, we have studied the angular distributions of $B^+ \rightarrow \phi\phi K^+$ decays below and within the η_c resonance. We conclude from these studies that the nonresonant $B^+ \rightarrow \phi\phi K^+$ events below the η_c resonance are, on average, more consistent with $J^P = 0^+$ than $J^P = 0^-$, while the distributions within the η_c resonance region are all consistent with $J^P = 0^-$.

ACKNOWLEDGMENTS

We are grateful for the extraordinary contributions of our PEP-II colleagues in achieving the excellent luminosity and machine conditions that have made this work possible. The success of this project also relies critically on the expertise and dedication of the computing organizations that support *BABAR*. The collaborating institutions wish to thank SLAC for its support and the kind hospitality extended to them. This work is supported by the US Department of Energy and the National Science Foundation, the Natural Sciences and Engineering Research Council (Canada), the Commissariat à

TABLE V. $B^+ \rightarrow 5K$ yield fit results for the five zones (B^+ yield column) and yields derived from the fraction matrix f_{ij} . The last row is computed from the inverted fraction matrix f_{ij}^{-1} and the B^+ yield column. The remaining 5×5 yield matrix was computed from the last row and the fraction matrix f_{ij} . The uncertainties are from propagating the statistical errors from the fitted region yields (B^+ yield column) without including any uncertainties on the fraction matrix.

Zone	B^+ yield	$\phi\phi K^\pm$	ϕKKK^\pm	$KKKKK^\pm$	$f_0\phi K^\pm$	f_0KKK^\pm
1	188.4 ± 16.0	183.2 ± 17.0	6.3 ± 3.9	0.8 ± 0.8	0 ± 3.0	0.3 ± 1.5
2	84.4 ± 18.0	36	39	9	-1.4	2
3	49.7 ± 19.0	3.8	18	26	-0.2	2.2
4	1.0 ± 2.0	1.3	0.9	0.2	-1.7	0.3
5	3.5 ± 5.0	0.2	0.8	1.3	-0.2	1.3
1-5		225 ± 21	65 ± 40	38 ± 38	-5.7 ± 7.6	6.2 ± 26

TABLE VI. $B^0 \rightarrow 5K$ yield fit results for the five zones (B^0 yield column) and yields derived from the fraction matrix f_{ij} . The last row is computed from the inverted fraction matrix f_{ij}^{-1} and the B^0 yield column. The remaining 5×5 yield matrix was computed from the last row and the fraction matrix f_{ij} . The uncertainties are from propagating the statistical errors from the fitted region yields (B^0 yield column) without including any uncertainties on the fraction matrix.

Zone	B^0 yield	$\phi\phi K_s^0$	ϕKKK_s^0	$KKKKK_s^0$	$f_0\phi K_s^0$	$f_0KKK_s^0$
1	43.4 ± 8.0	42.8 ± 8.4	1.2 ± 1.5	0.1 ± 0.3	0 ± 0.7	0 ± 0.02
2	15.1 ± 7.0	8	7	0.9	-0.4	-0.4
3	6.0 ± 6.0	1	3	2.5	-0.1	-0.4
4	0 ± 0.5	0.3	0.2	0	-0.5	0
5	0 ± 0.8	0	0.1	0.1	0	-0.2
1-5		52 ± 10	12 ± 15	3.6 ± 12	-1.6 ± 1.8	-1.1 ± 4.3

l'Energie Atomique and Institut National de Physique Nucléaire et de Physique des Particules (France), the Bundesministerium für Bildung und Forschung and Deutsche Forschungsgemeinschaft (Germany), the Istituto Nazionale di Fisica Nucleare (Italy), the Foundation for Fundamental Research on Matter (The Netherlands), the Research Council of Norway, the Ministry of Education and Science of the Russian Federation, Ministerio de Ciencia e Innovación (Spain), and the Science and Technology Facilities Council (United Kingdom). Individuals have received support from the

Marie Curie IEF program (European Union), the A.P. Sloan Foundation (USA), and the Binational Science Foundation (USA-Israel).

APPENDIX: PEAKING BACKGROUND ZONE FIT RESULTS

The results of the fits of the $B \rightarrow 5K$ yield in the five zones in the m_{ϕ_2} vs m_{ϕ_1} plane (shown in Fig. 2) and the derived yields for each of the five B decay modes are given in Tables V and VI below.

-
- [1] A. D. Sakharov, Pis'ma Zh. Eksp. Teor. Fiz. **5**, 32 (1967).
 [2] B. Aubert *et al.* (The BABAR Collaboration), Nucl. Instrum. Methods Phys. Res., Sect. A **479**, 1 (2002).
 [3] A. Abashian *et al.* (The Belle Collaboration), Nucl. Instrum. Methods Phys. Res., Sect. A **479**, 117 (2002).
 [4] PEP-II Conceptual Design Report, Report No. SLAC-0418 (1993).
 [5] S. Kurokawa and E. Kikutani, Nucl. Instrum. Methods Phys. Res., Sect. A **499**, 1 (2003).
 [6] M. Kobayashi and T. Maskawa, Prog. Theor. Phys. **49**, 652 (1973).
 [7] V. A. Rubakov and M. E. Shaposhnikov, Phys. Usp. **39**, 461 (1996).
 [8] Y. Grossman and M. P. Worah, Phys. Lett. B **395**, 241 (1997).
 [9] M. Hazumi, Phys. Lett. B **583**, 285 (2004).
 [10] H. C. Huang *et al.* (The Belle Collaboration), Phys. Rev. Lett. **91**, 241802 (2003); Y. T. Shen, K. F. Chen, (The Belle Collaboration), arXiv:0802.1547.
 [11] B. Aubert *et al.* (The BABAR Collaboration), Phys. Rev. Lett. **97**, 261803 (2006).
 [12] S. Fajfer, T. N. Pham, and A. Prapotnik, Phys. Rev. D **69**, 114020 (2004).

- [13] C.-H. Chen and H.-n. Li, *Phys. Rev. D* **70**, 054006 (2004).
- [14] Charge-conjugate states are implicitly included throughout the paper unless stated otherwise.
- [15] Throughout the paper, necessary factors of c are implied in the units for energy, mass, and momentum.
- [16] D. Lange, *Nucl. Instrum. Methods Phys. Res., Sect. A* **462**, 152 (2001).
- [17] S. Agostinelli *et al.* (The Geant4 Collaboration), *Nucl. Instrum. Methods Phys. Res., Sect. A* **506**, 250 (2003).
- [18] G. Fox and S. Wolfram, *Phys. Rev. Lett.* **41**, 1581 (1978).
- [19] B. Aubert *et al.* (The BABAR Collaboration), *Phys. Rev. D* **79**, 072009 (2009).
- [20] In each event one of the ϕ candidates is randomly chosen to be ϕ_1 with the other ϕ_2 . All aspects of the analysis, such as the PDFs used in the likelihood fits, are symmetric under the exchange of the ϕ_1 and ϕ_2 assignments (e.g. $m_{\phi_1} \leftrightarrow m_{\phi_2}$).
- [21] J. E. Gaiser, Ph. D. thesis, Stanford University [Institution Report No. SLAC-R-255, 1982, (unpublished)].
- [22] With $x \equiv m_{ES}/E_{beam}^*$ and ξ a parameter to be fitted, $f(x) \propto x\sqrt{1-x^2} \exp[-\xi(1-x^2)]$. See H. Albrecht *et al.* (The ARGUS Collaboration), *Phys. Lett. B* **241**, 278 (1990).
- [23] K. Nakamura *et al.* (The Particle Data Group), *J. Phys. G* **37**, 075021 (2010).
- [24] Z. Bai *et al.* (The Mark III Collaboration), *Phys. Rev. Lett.* **65**, 1309 (1990).
- [25] M. Ablikim *et al.* (The BES Collaboration), *Phys. Lett. B* **662**, 330 (2008).
- [26] M. Pivk and F. R. Le Diberder, *Nucl. Instrum. Methods Phys. Res., Sect. A* **555**, 356 (2005).